Appendix N: Assessment of Embedded Defects

1 Overview

The metallographic examination of sections from the Period C tanker J3910 revealed no evidence of surface flaws. The only circumferential defects that were identified were embedded defects due to either lack of side wall fusion or lack of root fusion. Typically, the total height of these defects was less than 1.0mm. A detailed analysis of the stability of such flaws was not undertaken in the previous TWI research programme (TWI, 2014).

In order to provide an analytical assessment of the fracture and fatigue acceptability of these defects, multiple embedded defects have been assessed with the dimensions inferred from the experimental measurements from J3910 and other Period C tankers. Additionally, in the absence of the observation of more severe defect dimensions, hypothetical 'worst-case' defects have been modelled to provide an estimate of the relative safety of the observed embedded defects against more severe defects.

2 Objectives

- To assess the stability of embedded defects under topple test conditions.
- To assess the fatigue crack growth of embedded defects in a GRW joint.

3 Approach

3.1 Software

All finite element models were generated using version 6.14-1 of the pre-processing finite element software Abaqus/CAE and the analyses were solved using version 6.14-1 of Abaqus/Standard (SIMULIA, 2014).

3.2 Geometry

The model geometry comprises the extrusion band profile, two lengths of tanker shell (either side of the extrusion band), and a bulkhead (Figure N1). The underlying geometry is an axisymmetric model of the GRW tanker band joint. The mean radius of the tanker joint model was assumed to be 2000mm, approximately equal to the average of the major and minor axes of the tanker along the length of the tanker. The nominal tanker shell wall thickness was 5.0mm. The extrusion band profile was provided to TWI by GRW as an AUTOCAD sketch that was imported into Abaqus/CAE and used to define the axisymmetric part. A bulkhead was modelled based upon the engineering drawings of various GRW tankers provided to TWI.

For the present study, the average joint geometry was employed as defined in the main report. Therefore, the weld cap height was 1.97mm, the weld cap width 15.6mm and the axial misalignment was 0.63mm.

The macros from J3910 were used to identify location, size and orientation of embedded defects. A typical embedded defect is shown in Figure N2. Based on assessment of macros from J3910 and J3564, it was determined that the two positions and orientations where embedded defects were most likely to occur were positions A and B as shown in Figure N3. In this figure:

- Position A is an embedded defect approximately 4-5mm offset in the axial direction from the left most weld toe of the circumferential weld. The orientation has been taken to be up-down, ie constant axial position for the crack plane. Although the fusion line is typically angled, it is more severe to

assume the flaw is normal to the applied load that is transferred through the tanker shell. Two flaws were modelled at Position A: one with height 2a = 1.0mm (Case A1) and one with height 2a = 3.0mm (Case A3). The position of the lower crack tip (ie the crack tip furthest from the outer surface of the extrusion band joint) was kept constant and was aligned with the inner surface of the tanker shell. No defects larger than 1.0mm were observed at Position A in any macros of GRW extrusion band joints and therefore Case A3 is taken to be a hypothetical, severe case.

- Position B is an embedded defect approximately 1.5mm offset in the axial direction from the positioner lip. The orientation at this location has been taken to be left-right, ie constant radial position for the crack plane. Three flaws were modelled at Position B: one with height 2a = 1.0mm (Case B1), one with height 2a = 2.0mm (Case B2), and one with height 2a = 3.0mm (Case B3). The position of the right most crack tip (ie the one closest to the tanker shell and visible misalignment gap) was kept constant at 1.5mm. No defects larger than 1.0mm were observed at Position B in any macros of GRW extrusion band joints, therefore Cases B2 and B3 is taken to be a hypothetical, severe case.

The flaws were modelled as sharp, seam cracks in Abaqus. No contact was modelled along the crack flanks and therefore it was possible to observe unphysical interpenetration of the crack flanks under compressive loading. Such deformation would result in negative crack driving force (ie negative values of J-integral and mode-I stress intensity factor). If and when this occurred, it was recorded and taken into consideration when assessing the flaws.

The axisymmetric assumption in the model implies that the flaws under consideration are fully-circumferential (or 'long' flaws in the terminology of BS 7910). The assumption about fully-circumferential flaws is detailed in the main report.

The additional internal fillet weld was not included in the models based upon the same considerations detailed in Appendix L.

Once the geometry had been defined, the entire model was meshed with quadrilateral, biquadratic, reduced integration, axisymmetric elements (type CAX8R in Abaqus). A spider web crack tip mesh was created with at least 10 rings of elements surrounding the crack tip. The innermost elements were modelled with collapsed and degenerate wedge elements. For the linear elastic simulations, the mid-side nodes of the innermost wedge elements were shifted to the quarter-point position and single-node degeneracy was employed to accurately resolve the $1/\sqrt{r}$ crack tip singularity (SIMULIA, 2014). For the elastic-plastic models, the mid-side nodes were left unshifted and duplicate node degeneracy was employed to allow for crack tip blunting. The finite element mesh was biased so as to be dense in the proximity of the defect and coarser away from the defect. A typical finite element mesh for the embedded defect study is shown in Figure N4.

3.3 Material properties

The tensile properties for the finite element simulations are as described in Appendix L with the tensile stress-strain curves shown in Figure N5. For the linear elastic simulations, the linear elastic constants for the model were 70,000MPa for the Young's modulus and 0.3 for Poisson's ratio.

3.4 Loads and boundary conditions

The primary objective is to determine the acceptability of embedded defects under the so-called topple test load case as described below.

As part of the Department for Transport research on petroleum tankers, the Health and Safety laboratory (HSL) undertook detailed fluid-structure interaction modelling of the topple testing of non-compliant GRW tankers. For the simulation involving the tanker filled with fuel oil and an initial rotational velocity of 2.6rad/s, HSL predicted that a section approximately 250mm long of the circumferential weld is acted on by a normalised bending moment of 1460N.mm/mm. This normalised bending moment defines the so-called 'topple test' load case. Assuming a Ramberg-Osgood representation of the stress-strain curve and a rectangular cross-section with length 1.0mm (unit length in the circumferential direction) and height 5.0mm (the tanker shell wall thickness), the through-wall, elastic-plastic bending stress generated by this moment is 254MPa. Taking into consideration that the HSL simulation employed the actual, non-circular cross-sectional geometry of the GRW tanker and that the TWI axisymmetric model assumed a circular cross-section with mean radius 2000mm, then in order to generate the same through-wall, elastic-plastic bending stress, the moment had to be modified accordingly. The modified, normalised moment for the circular cross-section was approximately 1630N.mm/mm.

A reference node was created in the model, aligned with the mean radius of the tanker shell on the leading end (ie the end in the negative y-direction). The axial degree of freedom of the nodes on the end face of the tanker shell was kinematically coupled to the reference node and the modified, concentrated moment was applied at the reference node. All other degrees of freedom except for the rotational degree of freedom about the z-axis were restrained at the loading reference node. The trailing end of the tanker shell (ie the end in the positive y-direction) was restrained in the axial direction. All models were analysed under small strain assumptions.

For each flaw modelled, the following load cases were analysed:

- Linear elastic analysis under topple test load case to calculate the primary stress intensity factor. Here, the primary stress intensity factor was taken to be the primary **effective** stress intensity factor due to the presence of mixed-mode loading.
- Linear elastic analysis assuming yield magnitude residual stresses. Independent of the orientation of the flaw, a load case was considered whereby a 133MPa crack flank pressure was applied and the resulting stress intensity factor was calculated to give K_I-secondary.
- Elastic-plastic analysis under topple test load case. This case was used to determine the elastic-plastic J-integral as a function of applied moment. In this case, the ultimate applied load was set to be 10 times greater than the actual topple test load to facilitate calculation of the load ratio L_r by using J-based methods. For a detailed description of the J-based method for calculating L_r, see previous reports by TWI (2013a and 2013b).

4 Results

4.1 Deformation behaviour of embedded defects

The primary applied load is a through-wall, elastic-plastic bending stress in the tanker shell that has nominal wall thickness equal to 5mm. However, all of the embedded defects that have been analysed are located away from the tanker

shell, well within the thicker (10-15mm) extrusion band region. As a consequence, the through-wall bending stress redistributes as it enters the thicker section of the extrusion band. On top of this stress redistribution, axisymmetric bending is secondary in nature in that it does not arise from a global applied bending moment. Consequently, the through-wall bending stress associated with a local bending moment about the circumferential coordinate decays with distance to the applied moment. The net effect is that all of the embedded defects analysed are in a region that is significantly less stressed than the surface-breaking defects analysed in the main report.

This is illustrated for the Position A flaws in Figure N6 and Figure N7 and for the Position B flaws in Figures M8-M10. It can be seen from these figures that the overall crack mouth opening is very low and that most of the flaws are positioned in a region where the von Mises stress is approximately 50-100MPa which is about 20-40% of the applied stress.

4.2 Failure assessment diagram calculations

As described in Section 3.4, for each flaw modelled, the primary stress intensity factor and the secondary stress intensity factor were determined. These values were then combined as described in the main report to determine the fracture ratio K_r, taking into account the plasticity interaction correction factor ρ where appropriate and the fracture toughness obtained from sub-size SENB fracture toughness testing (Appendix H). The elastic-plastic simulation of the topple test load case was used to calculate J_{ep} (ie J-elastic-plastic) as a function of applied moment. The corresponding linear elastic J-integral, J_e, was also evaluated for the topple test load case. These two values were combined to plot $\sqrt{(J_e/J_{ep})}$ as a function of applied moment. The collapse moment was taken to be the applied moment at which the value of $\sqrt{(J_e/J_{ep})}$ equalled the value of K_r from the Option 2 failure assessment diagram at $L_r = 1$. Dividing the total applied moment by the collapse moment gives the load ratio, L_r. This is illustrated in Figure N11 for Case B1. Note that, as with previous surface-breaking flaw cases, it was not possible to evaluate the J-based limit moment in all cases. This occurred in Case A1 because the gross plastic straining of the tanker shell resulted in non-convergence of the FE simulation. For this case, the limit moment was taken conservatively to be the largest moment for which the simulation converged. This is expected to be conservative, because the J-based limit moment had not yet been reached.

A failure assessment diagram is shown in Figure N12. Where two symbols are shown for the same case, it means that both crack tips of the embedded defect are in tension and have been assessed. Where there is only one symbol present for a given case, it means that one of the crack tips was in compression. It can be seen that all points are within the acceptable region of the failure assessment diagram and thus are deemed safe. Even the most severe defects, Cases A3, B2 and B3, which were hypothetical cases having total defect height more than two-to-three times the largest observed defect height, are safe.

4.3 Fatigue crack growth calculations

In order to determine likelihood for failure arising from fatigue crack growth from an initial embedded defect at Position A or Position B, fatigue crack growth calculations were undertaken. The fatigue crack growth law and the fatigue stress spectrum are described in detail in Section 3 and 4.6 of the main report.

For each of the geometries under consideration, a 1MPa membrane stress was applied to the tanker shell and the resulting stress intensity factors were calculated at each crack tip for the embedded flaws. The mode-I and mode-II

stress intensity factors were then combined to calculate the effective stress intensity factor. Taking into account linear superposition, for a given flaw, the effective stress intensity factor under a 1MPa membrane stress was multiplied by a factor of 20 to determine the stress intensity factor due to a 20MPa membrane stress, the approximate upper bound of meaningful stress range cycles obtained from the fatigue data collection exercise. Assuming that the stress range of 20MPa involves a maximum stress of 20MPa and minimum stress of 0MPa, then these stress intensity factors correspond directly with the stress intensity range due to a 20MPa membrane stress cycle, and the values are shown in Table M1.

As noted in Section 4.6 of the main report, no fatigue crack growth occurs for stress intensity ranges below the stress intensity range threshold, ΔK_{th}, which for the aluminium alloy under consideration was taken to be 21.3MPa$\sqrt{mm}$. In Table M1, all embedded defects except for case A3 (ie an embedded defect with height, 2a = 3mm, at Position A) have $\Delta K_{eff} < \Delta K_{th}$, hence no fatigue crack growth would occur. This agrees with the metallographic examination of sections from J3910 in which no evidence of fatigue crack growth of the embedded defects was observed.

When fatigue crack growth calculations are undertaken for Case A3, assuming the average joint geometry and pure membrane fatigue stress cycles, the calculated fatigue life is in excess of 25 years (where a 'year' is taken to mean 220,000km of travel). Therefore, even if an embedded defect such as Case A3 were to exist, it would not lead to likely failure during normal operating conditions and a typical UK duty cycle by fatigue crack growth. However, no embedded defect has been observed at Position A with total height greater than 1.0mm.

5 Conclusions

A series of measured and hypothetical fully-circumferential embedded defects have been assessed to determine the likelihood of failure under topple test load conditions and due to fatigue crack growth. It was determined that all five embedded defects were safe under topple test conditions. All defects except for Case A3 would not grow by fatigue due to the low effective stress intensity factor. It was determined that, conservatively assuming all fatigue stress cycles are pure membrane stress, that Case A3 would take in excess of 25 years to result in failure by fatigue crack growth.

6 References

SIMULIA (2014): 'Abaqus Analysis User's Manual'

TWI (2013a): 'Short-term Fitness for Service Assessment of GRW Road Tankers, TWI (Draft) Report 23437/1/13, September 2013.

TWI (2013b): 'Project 23437 Contract Amendment: Additional FEA for assessment of GRW road tankers, TWI (Draft) Report 23437/2/13, October, 2013.

TWI (2014): 'Department for Transport Technical Assessment of Petroleum Tankers: Work Package 2 – Detailed Engineering Critical Assessment', TWI Report 24000/8/4, 26 November 2014.

Table 1 Effective stress intensity factor range (ΔK_{eff}) due to a 20MPa membrane stress cycle.

Embedded defect ID	ΔK_{eff} at tip 1 (MPa$\sqrt{mm}$)	ΔK_{eff} at tip 2 (MPa$\sqrt{mm}$)
A1	14.83	13.52
A3	33.64	29.92
B1	4.47	5.45
B2	4.69	7.25
B3	4.25	8.40

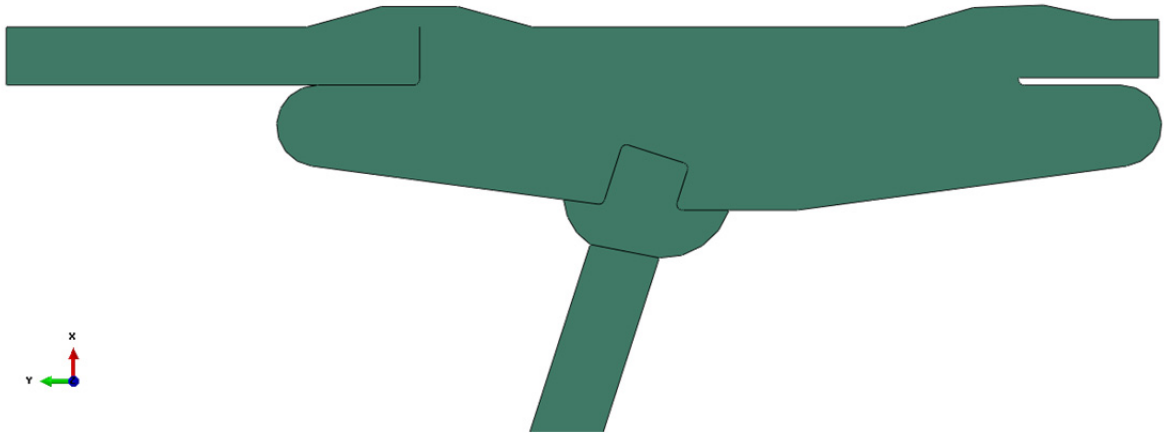

Figure N1 Diagram of the geometry of the GRW extrusion band joint under consideration.

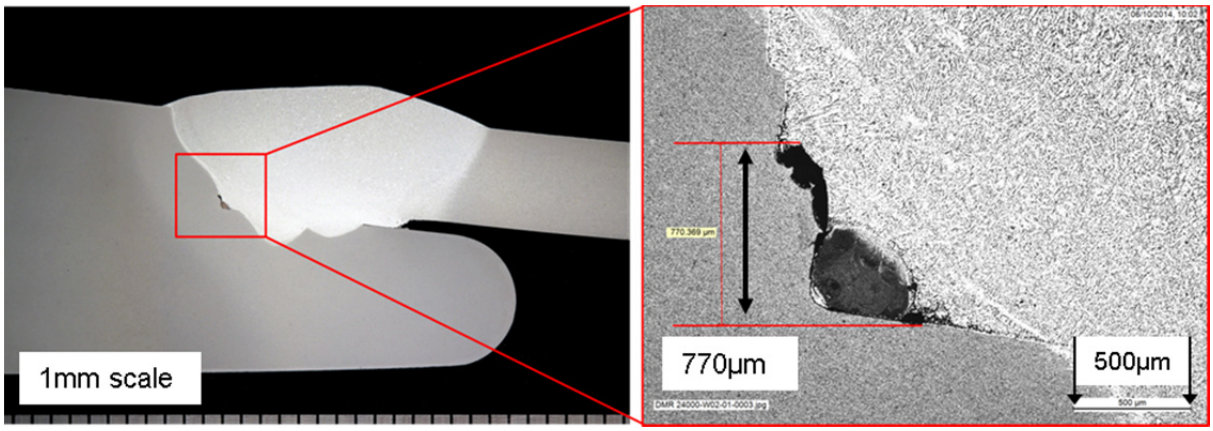

Figure N2 Typical embedded defect found in J3910. Macro W03-01 for J3910. The flaw shown has total height about 0.78mm.

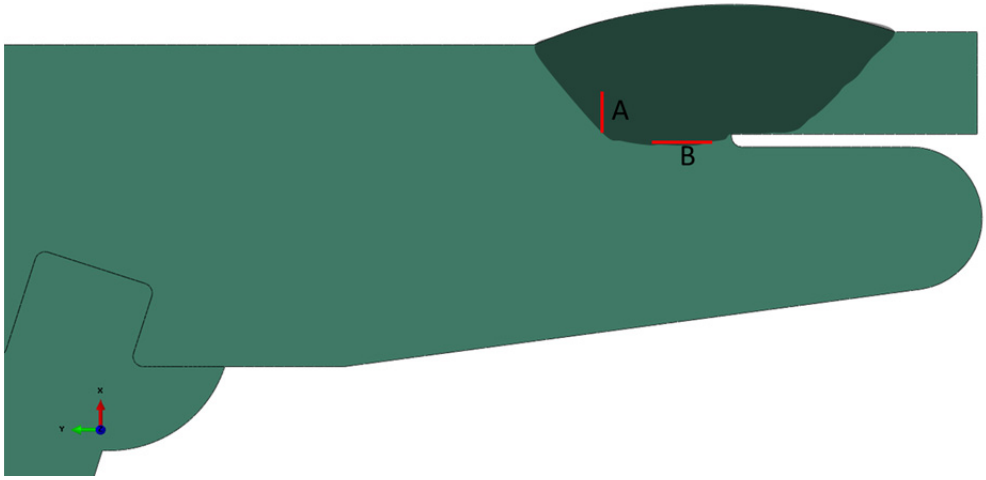

Figure N3 Diagram of the positions and orientation of the hypothetical flaw locations A and B.

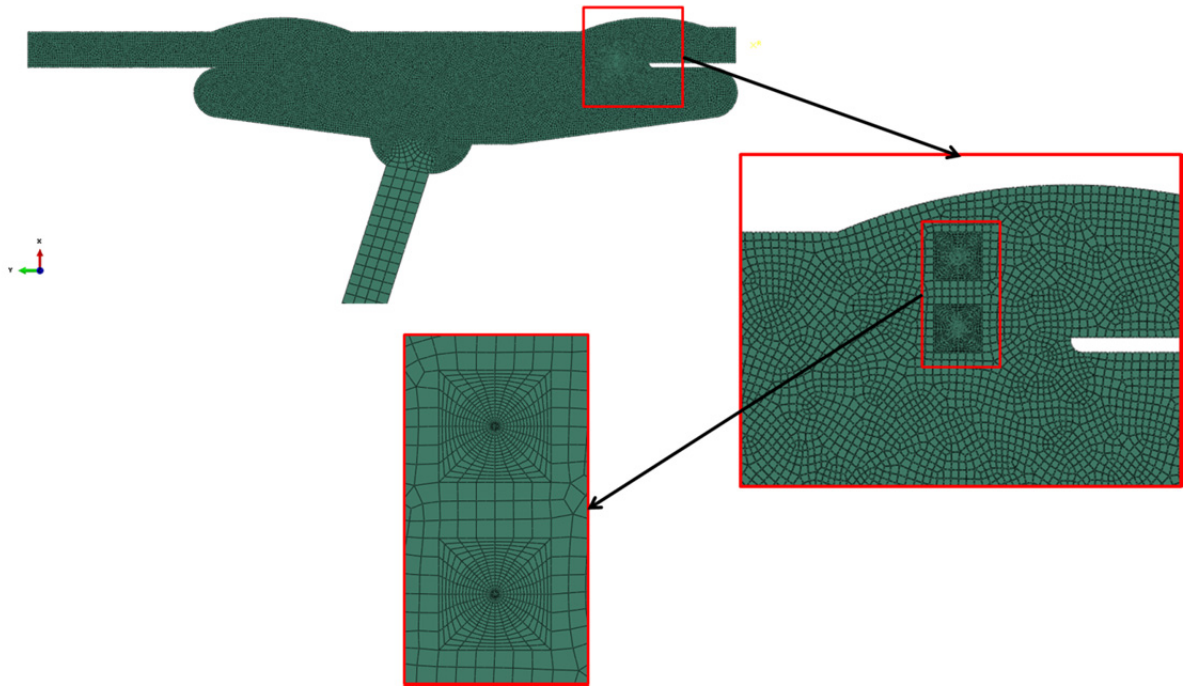

Figure N4 Illustration of a typical finite element mesh with Case A3 shown above.

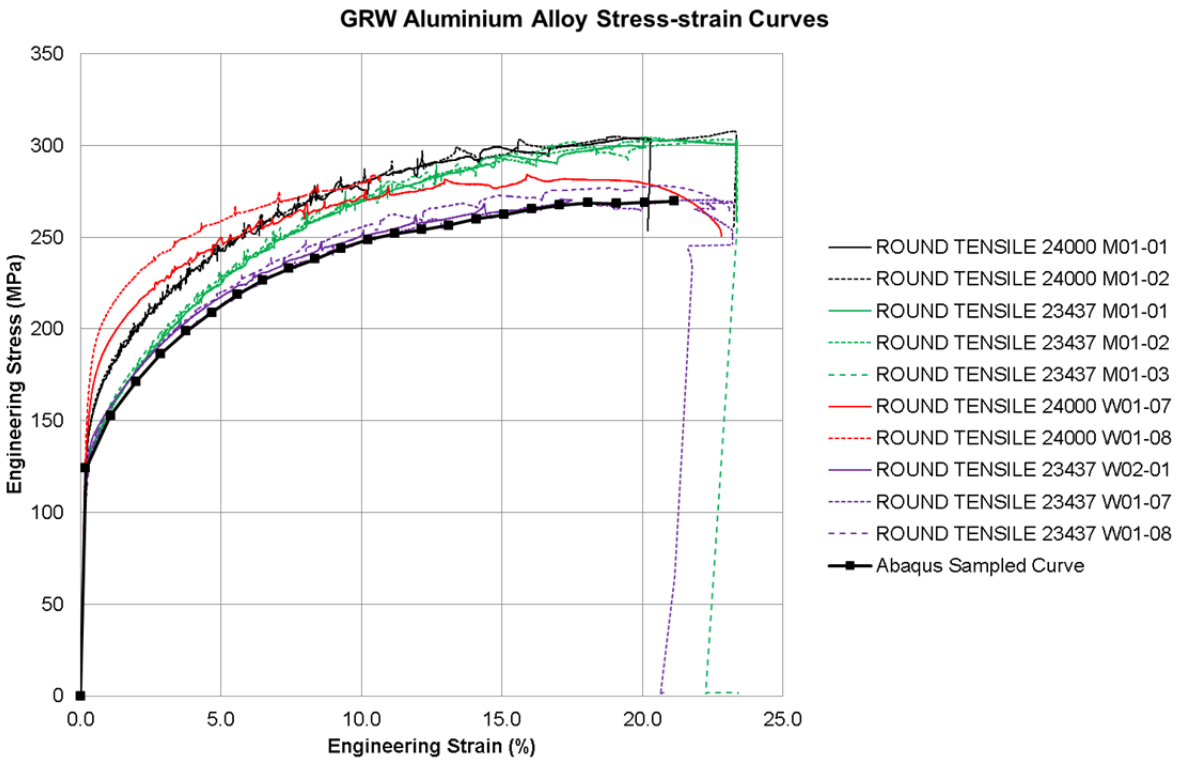

Figure N5 Tensile stress-strain curves for parent and weld metal. Black dark line shows the sampled data points used for the finite element models.

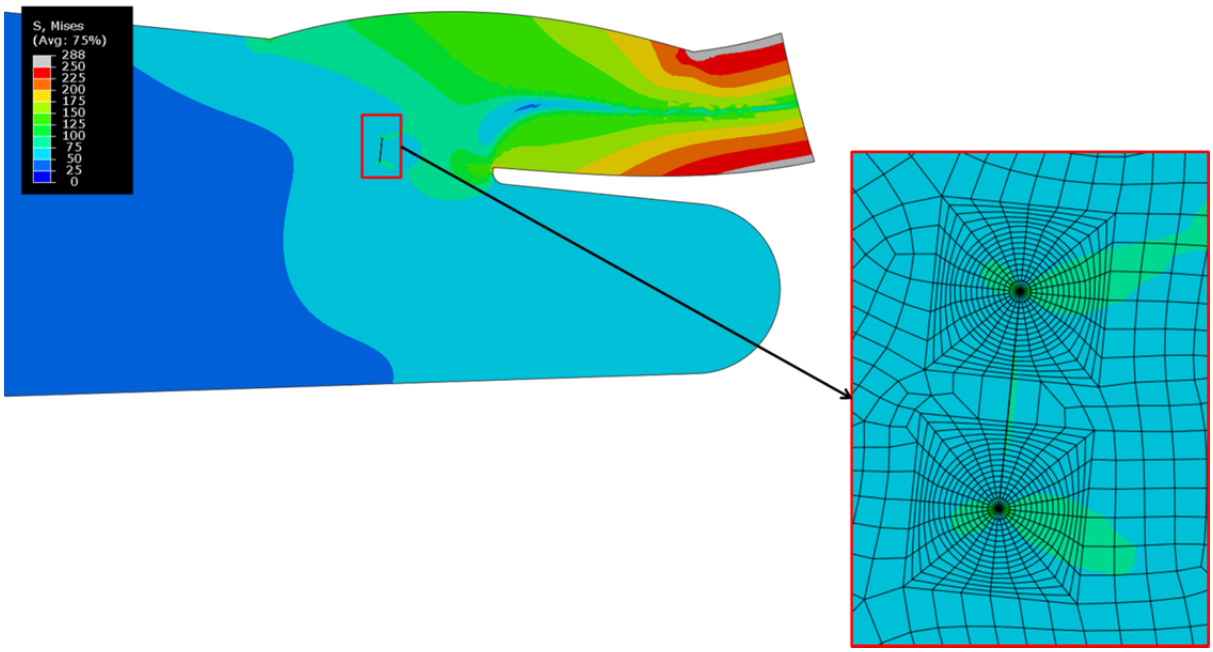

Figure N6 Von Mises stress contour for Case A1 under elastic-plastic topple test load case. Deformation scaled x2. Note the defect is in a region of relatively low stress (50Mpa) compared with the applied stress of 254MPa.

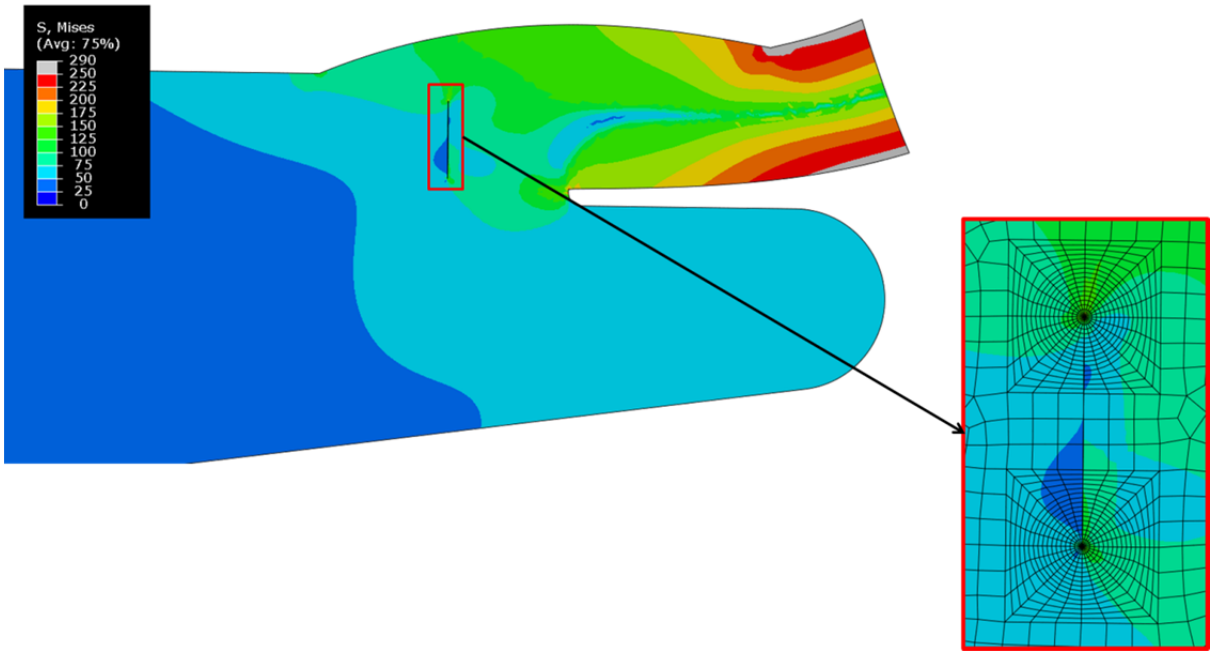

Figure N7 Von Mises stress contour for Case A3 under elastic-plastic topple test load case. Deformation scaled x2. Here, one of the crack tips (the outermost) is in a region of compressive stress that results in crack closure.

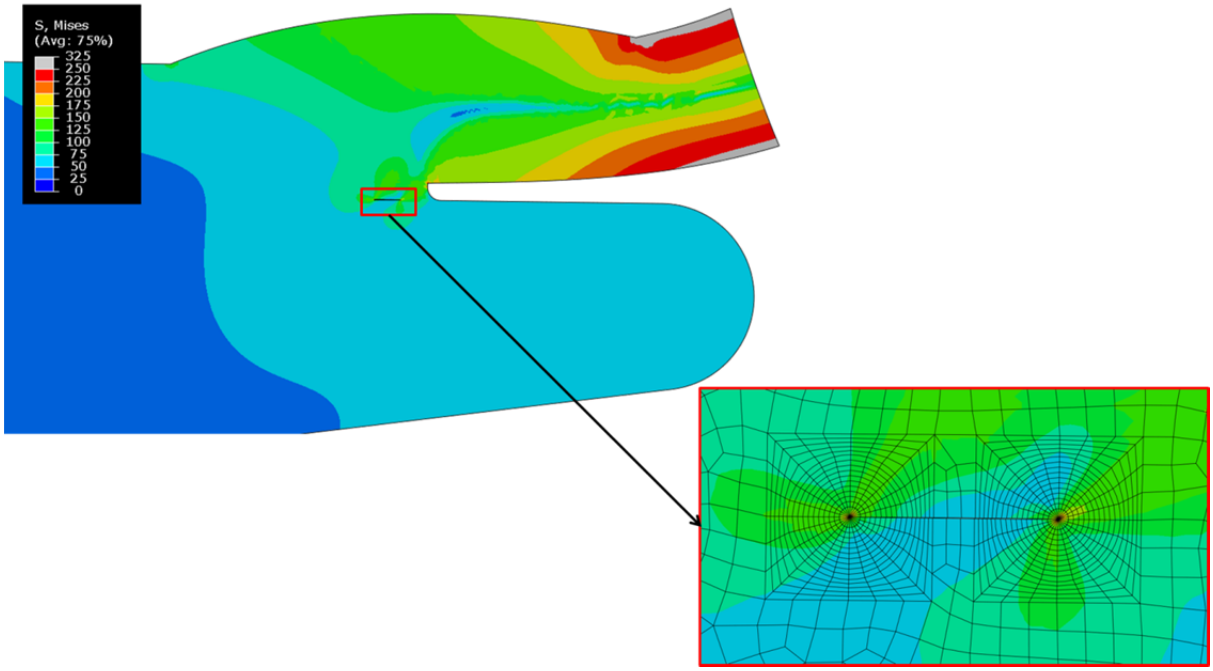

Figure N8 Von Mises stress contour for Case B1 under the elastic-plastic topple test load case.

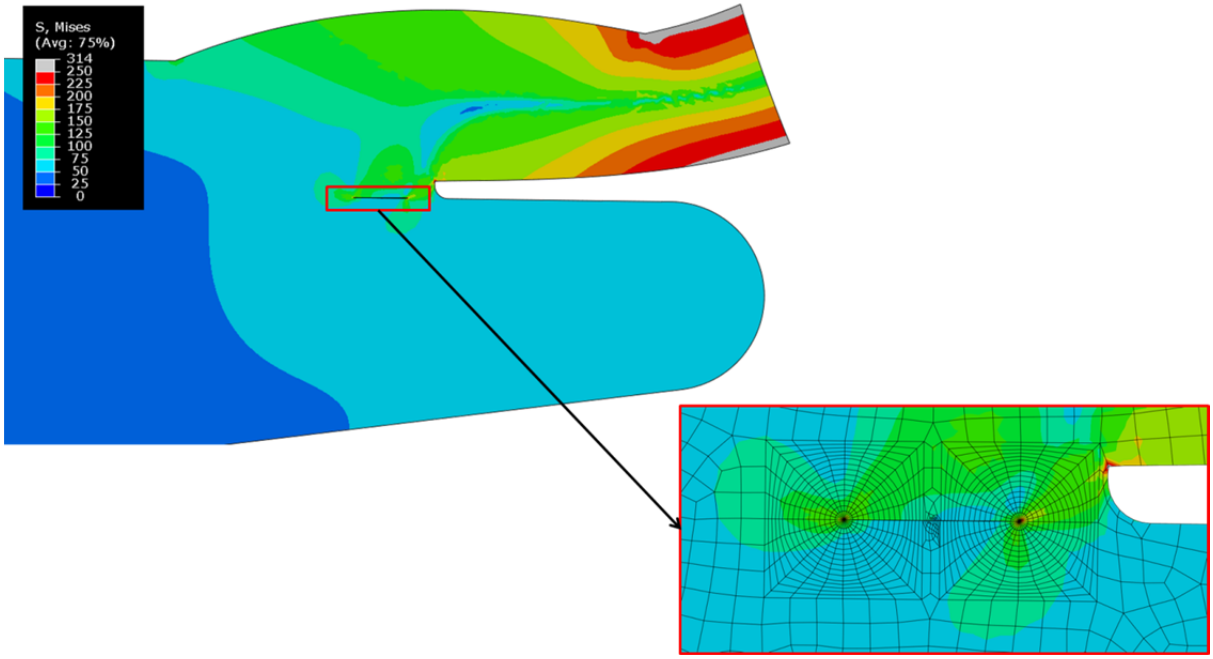

Figure N9 Von Mises stress contour for Case B2 under the elastic-plastic topple test load case.

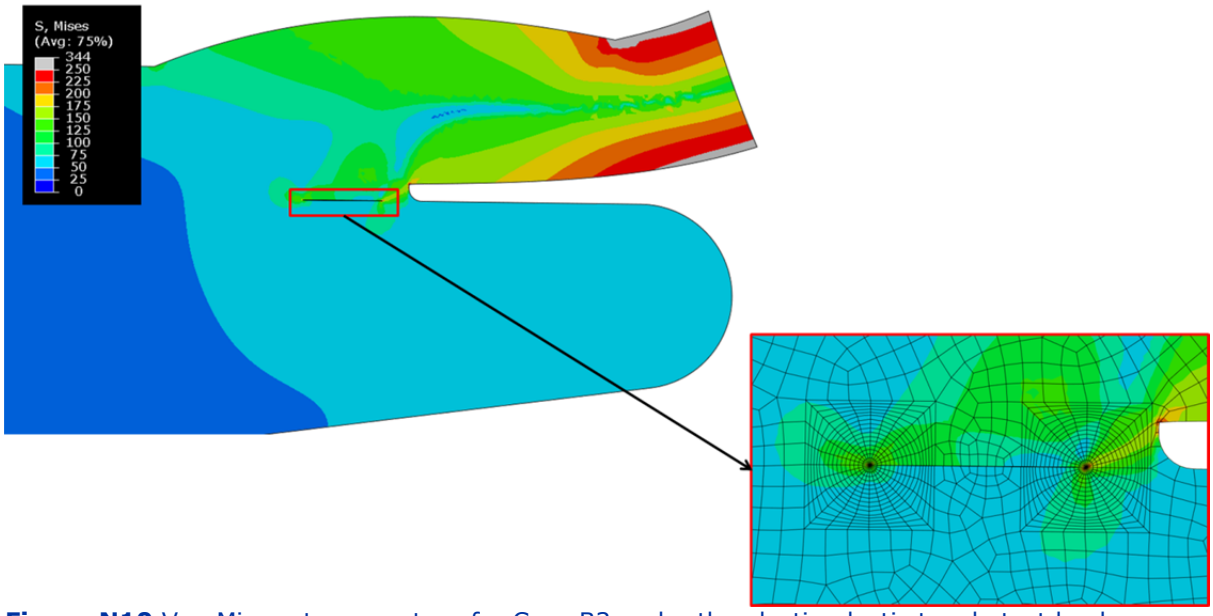

Figure N10 Von Mises stress contour for Case B3 under the elastic-plastic topple test load case.

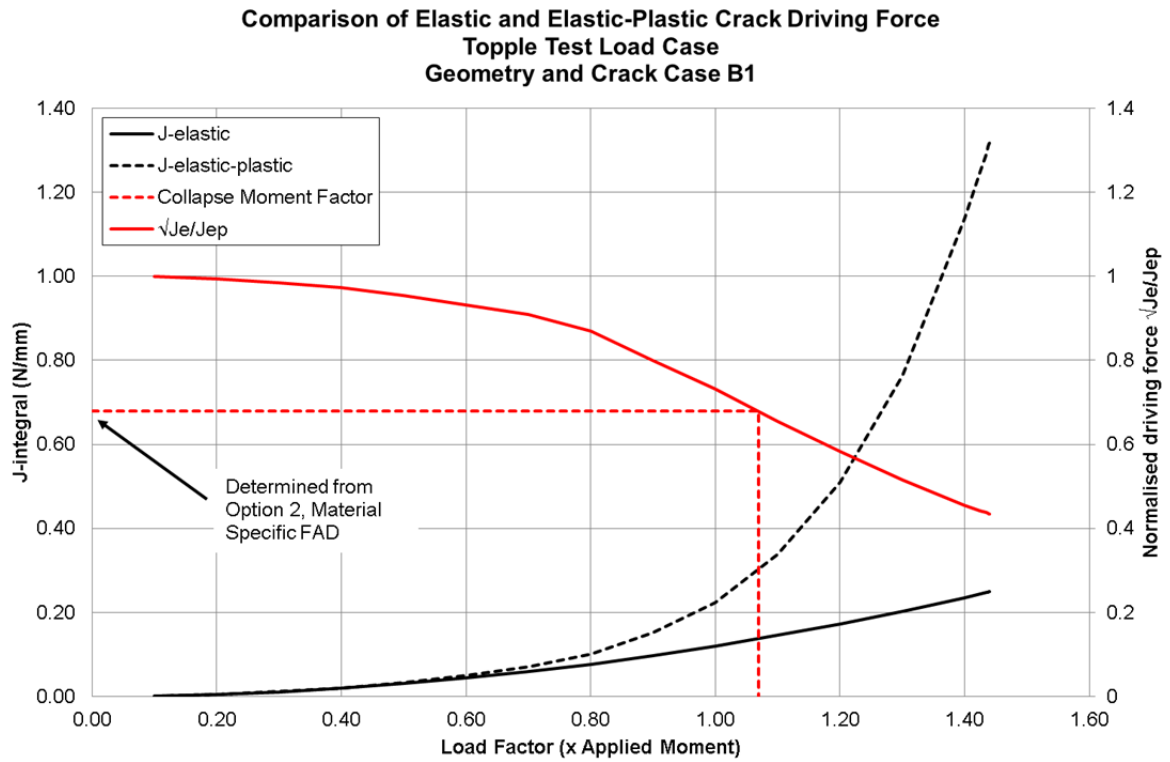

Figure N11 Illustration of the J-based limit moment calculation for Case B1.

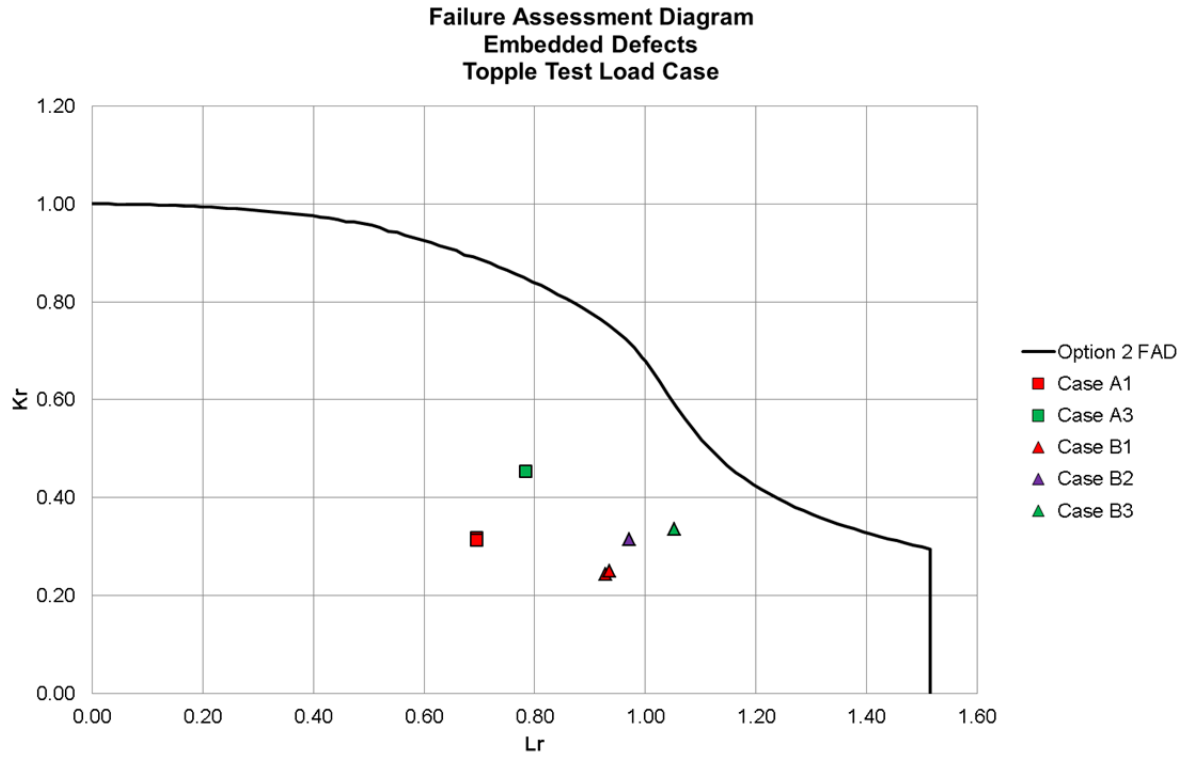

Figure N12 Failure assessment diagram for the embedded defects at Position A and Position B.